Theoretical modelling of XBn T2SLs InAs/InAsSb/B-AlAsSb mid-wave detector operating below thermoelectrical cooling

P. Martyniuk [a,*], K. Michalczewski [a], T.Y. Tsai [b], C.H. Wu [b], Y.R. Wu [b]

[a] Institute of Applied Physics, Military University of Technology, 2 Gen. S. Kaliskiego St., 00-908 Warsaw, Poland
[b] Graduate Institute of Photonics and Optoelectronics, National Taiwan University, Roosevelt Rd., 10617 Taipei, Taiwan

ARTICLE INFO

ABSTRACT

The paper reports on the barrier mid-wave infrared InAs/InAsSb (x_{Sb} = 0.4) type-II superlattice detector operating below thermoelectrical cooling. AlAsSb with Sb composition, x_{Sb} = 0.97; barrier doping, $N_D <$ 2×10^{16} cm^{-3} leading to valence band offset below 100 meV in relation to the active layer doping, N_D = 5×10^{15} cm^{-3} was proved to be proper material not introducing extra barrier in valence band in the analyzed temperature range in XBn architectures. The detectivity of the simulated structure was assessed at the level of $\sim 10^{11}$ Jones at $T \sim 100$ K assuming absorber thickness, d = 3 μm. The detector's architecture for high frequency response operation, τ_s = 420 ps ($T \sim 77$ K) was presented with a reduced active layer of d = 1 μm.

1. Introduction

Infrared detectors have many applications in civilian and military environment. Currently, many of these infrared (IR) applications require high-performance Mercury Cadmium Telluride (MCT) photodetectors. Due to higher cost of the MCT, antimonide-based type-II superlattices (T2SLs) have been proposed as an alternative with lower fabrication cost and better performance with low dark current due to the suppressed Auger generation-recombination (GR) rate and tunneling current [1,2]. It must be underlined that those theoretical predictions have not been reached yet. The limiting factor of the widely studied T2SLs InAs/GaSb is short minority carrier lifetime. That could be circumvented by "Ga-free" T2SLs InAs/InAsSb revealing very encouraging results in terms of the carrier lifetime $\sim$ 400 ns due to the strong suppression of nonradiative recombination [3–5]. Except material, it has been demonstrated that the XBn structure suppresses the dark current in IR photodetectors effectively through bandgap engineering [6]. The barrier layer in the XBn structure plays a decisive role and must be properly chosen in relation to the absorber layer in order not to introduce valence band offset (VBO) impeding carrier transport. In this paper, we demonstrate theoretical modelling of MWIR XBn photodetectors with T2SLs InAs/InAsSb active layer where the AlAsSb barrier was incorporated for operating below

thermoelectrical cooling. The detailed analysis of the barrier layer Sb composition (x_{Sb}) and doping (n-type, N_D) is presented. In addition two architectures with n- and p-type doping cap layers are being considered. It is shown that AlAsSb with x_{Sb} = 0.97, n-type doping, $N_D < 2 \times 10^{16}$ cm^{-3} does not introduce extra barriers into the valence band of the T2SLs InAs/InAsSb XBn structure in relation to the n-type absorber, $N_D = 5 \times 10^{15}$ cm^{-3}.

2. Simulation procedure and results

The nominal simulated T2SLs InAs/InAsSb/B-AlAsSb barrier structure is presented in Fig. 1. Both T2SLs InAs/InAsSb contact layers (0.2 μm n/p-type, $N_{D/A} = 10^{16}$ cm^{-3} and 0.1 μm n-type 5×10^{17} cm^{-3}) and absorber (d = 3 μm - for detectivity optimization and d = 1 μm for high frequency response, $N_D = 5 \times 10^{15}$ cm^{-3}) were assumed to have 5.2 nm (InAs) and 1.2 nm (InAsSb) with Sb composition, x_{Sb} = 0.4 (T2SLs InAs/InAs$_{0.6}$Sb$_{0.4}$). The 0.1 μm, n-type, $N_D = 10^{16}$ cm^{-3} AlAsSb (x_{Sb} = 0.97) barrier was introduced to the detector's structure. That material is assumed not to introduce any additional valence band in analyzed XBn structure.

Ohmic contacts are implemented as a Dirichlet boundary conditions, where the surface potential and electron and hole quasi-Fermi are fixed. The quasi-Fermi potentials for the electron (E_{fn}) and holes (E_{fp}) are equal and set to the applied bias (V) of the electrode:

$$E_{fn} = E_{fp} = V. \tag{1}$$

* Corresponding author.
  E-mail address: piotr.martyniuk@wat.edu.pl (P. Martyniuk).

Table 1
Material parameters taken in modelling of T2SLs InAs/InAsSb (active layer and contact layers).

Parameters	Symbols	GaAs	InAs	InSb	GaSb
Lattice constant	a_T(Å/K)	3.88×10^{-5}	2.74×10^{-5}	3.48×10^{-5}	4.72×10^{-5}
$a(T)=a(T=300\,K)+a_T \times (T-300)$	$a(T=300\,K)$(Å)	5.65325	6.0583	6.4794	6.0959
Bandgap	α(meV/K)	0.5405	0.276	0.32	0.417
$E_g^{\Gamma}(T)=$	β(K)	204	93	170	140
$E_g^{\Gamma}(T=0\,K) - \frac{\alpha T^2}{T+\beta}$	$E_g^{\Gamma}(T=0\,K)$ (eV)	1.519	0.417	0.25	0.812
	γ_1	7.05	20.0	34.8	13.4
Luttinger parameters	γ_2	2.35	8.5	15.5	4.7
	γ_3	3	9.2	16.5	6
	a_c(eV)	−7.17	−5.08	−6.94	−7.5
Deformation potentials	a_v(eV)	−1.16	−1	−0.36	−0.8
	b(eV)	−2	−1.8	−2	−2
	d(eV)	−4.8	−3.6	−4.7	−4.7
	C_{11}(GPa)	1221	832.9	684.7	884.2
Elastic constant	C_{12}(GPa)	566	452.6	373.5	402.6
	C_{44}(GPa)	600	395.9	311.1	432.2
Spin-orbit energy	Δ_0(eV)	0.341	0.39	0.82	0.76
Kane potential	E_p(eV)	23.81	21.5	24.08	24.76
Electron affinity	χ(eV)	4.07	4.9	4.59	4.06
Valence band offset	VBO(eV)	−0.8	−0.59	0	−0.03
Effective mass (0 K)	$\frac{m_e^*}{m_0}$	0.064	0.023	0.0138	0.038
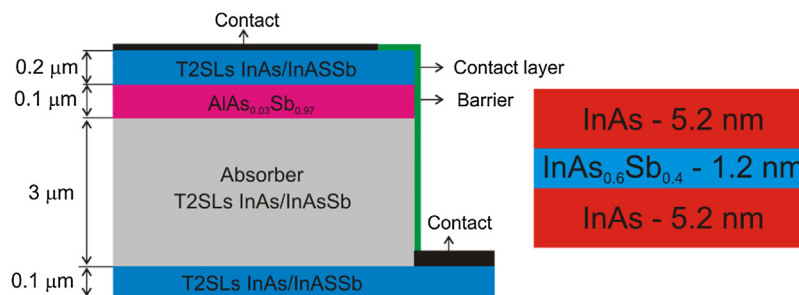
Fig. 1. MWIR T2SLs InAs/InAsSb/B-AlAsSb barrier detector.

Table 2
Bowing parameters for InAsSb.

Bowing parameters	E_g^{Γ}(eV)	0.67
	Δ_0(eV)	1.2
	$m_e^*(\Gamma)/m_0$	0.035
	Vacuum energy levels of the valence band $E_{v,vac}$(eV)	−0.47

Ohmic contacts in the simulation do not disrupt the area of simulation but allow a path for current flow.

In order to analyze the electro-optical properties (bandgap energy and effective masses in both plane and growth directions) of the T2SLs InAs/InAs$_{0.6}$Sb$_{0.4}$ for photodetector applications, we used the finite difference method to discretize a 8×8 kp Schrödinger Hamiltonian into a 8N×8N matrix. The periodic boundary condition was applied with 1 period to form the T2SLs InAs/InAsSb. With consideration of the strain effect into the kp Hamiltonian, the band structure was obtained. The bandgap, effective mass and absorption of T2SLs InAs/InAs$_{0.6}$Sb$_{0.4}$ are extracted from the dispersion curves. The absorption coefficient was calculated from the transition rate obtained by Fermi's Golden rule.

The material parameters assumed in T2SLs InAs/InAsSb modelling are presented in Tables 1 and 2 where bowing parameters for bandgap, spin-orbit energy, electron effective mass and vacuum energy levels of the valence band were shown while the XBn barrier architecture parameters are presented in Table 3, respectively [7].

The T2SLs InAs/InAsSb bandgap energy *vs.* temperature and fitted Varshni [E_g (0 K) = 0.26 eV, α = 2.5 × 10^{-4} K^{-1} and β = 34 K] equation are presented in Fig. 2(a) while electron and hole effective masses are presented in Fig. 2(b). Within the analyzed temperature range, E_g decreases from 0.245 eV to 0.222 eV which corresponds to the cut-off wavelength (λ_c), λ_c = 5.06 μm (80 K) and 5.60 μm (180 K). Electron effective mass decreases *vs.* temperature according to the relation:

$$m_e^*/m_0 = -2 \times 10^{-8}T^2 - 9 \times 10^{-6}T + 0.0202, \qquad (2)$$

while hole stays nearly constant:

$$m_h^*/m_0 = 2 \times 10^{-7}T^2 - 7 \times 10^{-5}T + 0.2133. \qquad (3)$$

The zero voltage carrier mobilities *vs.* temperature were simulated and the results are presented in Fig. 3(a). Electron mobility temperature dependence could be expressed by the relation:

$$\mu_e = 677.74 \times \left(1000/T\right)^{2.9978}, \qquad (4)$$

while hole mobility temperature dependence is given by the formula:

$$\mu_h = 0.3121 \times \left(1000/T\right)^{2.9867}. \qquad (5)$$

The zero bias mobility was calculated using the intrinsic semiconductor model. Those relations were incorporated into the Canali (Beta-model for the electric field-dependent mobility dependence) model in order to estimate carrier mobility function *vs.* voltage [8]:

$$\mu_{n,p} = \frac{\mu_{no,po}}{\left[\left(1 + \left(\frac{\mu_{no,po}F}{V}\right)^{B_{n,p}}\right)^{1/B_{n,p}}\right]}, \qquad (6)$$
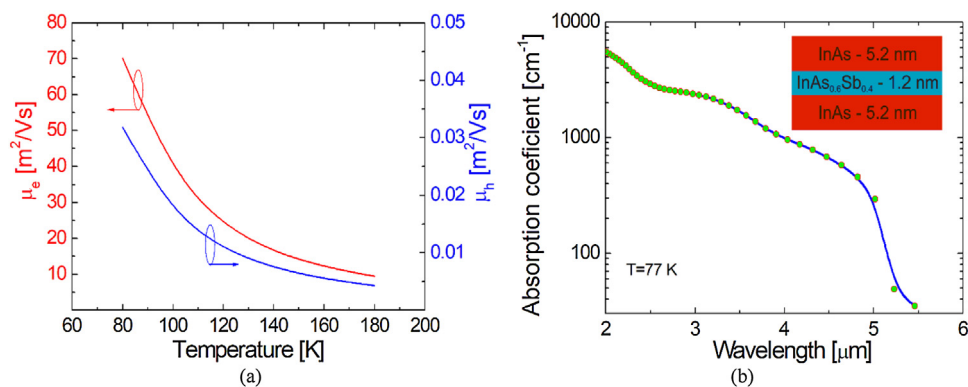
where: $\mu_{no,po}$ temperature dependence is presented in Fig. 3(a) - zero bias mobility, $B_n = 2$, $B_p = 1$, saturation electron velocity $V = 10^5$ m/s, normalizing electric field $F = 4 \times 10^5$ V/m. The Fermi's Golden

Table 3
Parameters assumed in XBn barrier detector simulation.

Parameters	Contact layer	Barrier layer		Absorber layer	Contact layer
Doping, $N_{D/A}$ cm^{-3}	$N_{D/A} = 10^{16}$	$N_D = 10^{16}$		$N_D = 5 \times 10^{15}$	$N_D = 5 \times 10^{17}$
Doping Gauss tail, dx μm	0.02	0.02		0.02	0.02
Composition (InAsSb, AlAsSb), x_{Sb}	0.4	0.97		0.4	0.4
Thickness, d μm	0.2	0.2		1–3	0.1
Electrical area, A μm^2	100×100				
Overlap matrix, F_1F_2	0.2	Auger coefficients: $C_n = 10^{-36}$ cm^6/s; $C_p = 10^{-36}$ cm^6/s		0.2	0.2
Trap energy level, E_{Trap}	$0.3 \times E_g$	$0.75 \times E_g$		$0.3 \times E_g$	$0.3 \times E_g$
Trap concentration, N_{Trap} cm^{-3}	10^{13}	10^{13}		10^{13}	10^{13}
SRH capture cross section, σ_n/σ_p cm^2	5×10^{-16}	10^{-16}		5×10^{-16}	5×10^{-16}
Incident power density, P W/m^2	1				
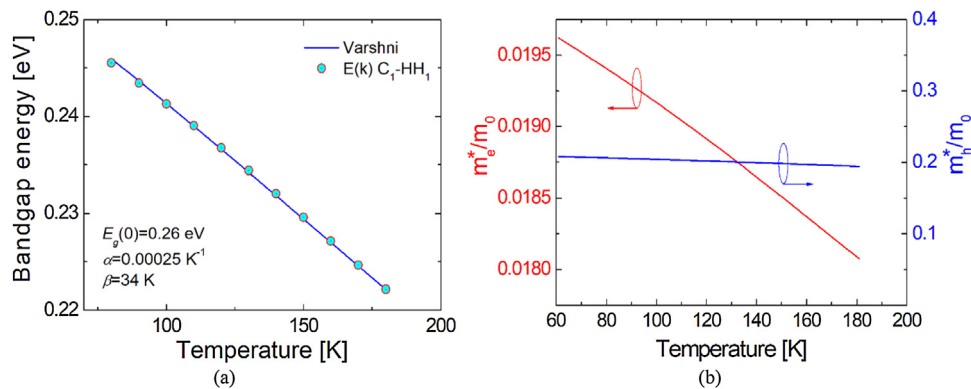
Fig. 2. T2SLs InAs/InAsSb bandgap energy (a) and electron/hole effective masses (b) *vs.* temperature.

Fig. 3. T2SLs InAs/InAsSb zero voltage carrier mobility *vs.* temperature (a) and absorption coefficient (b) versus wavelength at T = 77 K.

rule absorption coefficient dependence *vs.* wavelength is presented in Fig. 3(b) where for λ = 4 μm and T = 77 K assumes, α = 1000 cm^{-1}.

The barrier detector structure was simulated with software APSYS by Crosslight Inc. using the bulk based two band model. The simulation incorporates both T2SLs InAs/InAsSb and barrier AlAsSb electrical and optical properties to estimate device performance taking into consideration radiative (RAD), Auger (AUG), Shockley-Read-Hall (SRH) GR mechanisms.

The XBn detector parameters implemented into APSYS drift-diffusion (DD) model are presented in Table 3. The RAD and AUG GR for T2SLs InAs/InAsSb rates were calculated as the average of RAD and AUG GR for bulk InAs and InAsSb (x_{Sb} = 0.4). Overlap matrix, F_1F_2 for InAs and InAsSb AUG GR simulation was assumed at the level 0.2.

The proper choice of the barrier layer parameters to include doping and Sb composition in relation to the barrier layer is extremely important in terms of optimal performance of the XBn barrier detector. That is fully confirmed by Perez *et al.* where authors reported on T2SLs InAs/InAsSb with x_{Sb} = 0.35, non-intentionally

doped (nid), d_{InAs} = 4.1 nm, d_{InAsSb} = 1.4 nm MWIR [PL λ_c = 4.75 μm (T = 80 K), responsivity measurements 4.75–5.1 μm (T = 77–140 K)] barrier detector with AlAsSb (assumed x_{Sb} = 0.91, estimated x_{Sb} = 0.945, n-type doping, N_D = 10^{17} cm^{-3}) performance [9]. Below we present and confirm by theoretical simulation that barrier layer (x_{Sb} = 0.945, n-type doping, N_D = 10^{17} cm^{-3}) was not optimized to reach the utmost performance due to the reduction of the VBO.

The barrier layer's optimization *vs.* barrier composition and doping is presented in Fig. 4(a) and Fig. 4(b). Energy barriers in conduction band (E_C) and valence band (E_V) were simulated within the barrier composition range, x_{Sb} = 0.3–1 (barrier doping was assumed at the level of N_D = 10^{16} cm^{-3}).

The presented results directly indicate the optimal barrier composition. E_C increases *vs.* x_{Sb} (0.3–1) from 0.45 eV to 1.40 eV while E_V decreases within the range 0.920 eV to 0.042 eV.

The barrier doping influence is also important and the performed simulations indicate that E_V is minimized and E_C maximized when both barrier and absorber n-type doping are comparable. The applied voltage reduces E_C and E_V. According
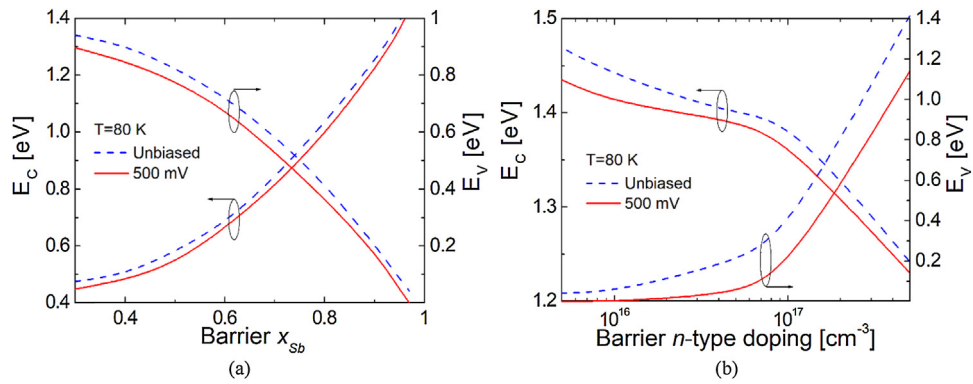
Fig. 4. E_C and E_V vs. barrier layer x_{Sb} (a) and n-type doping (b) at 80 K for unbiased and 500 mV condition.
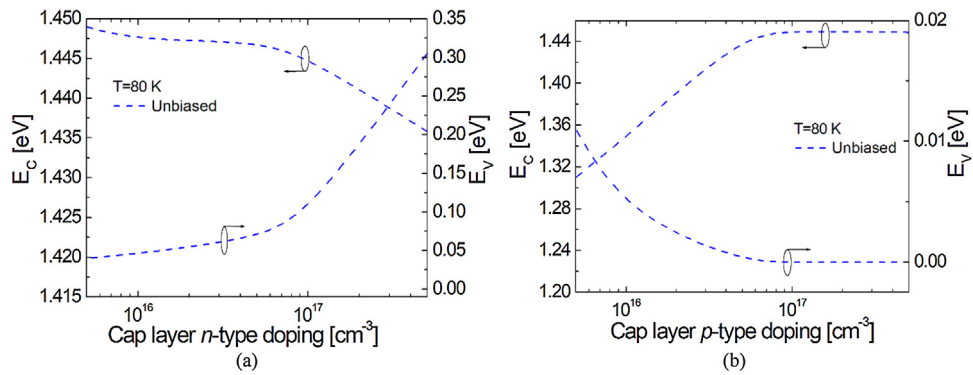

Fig. 5. E_C and E_V vs. cap layer n-type doping (a) and p-type doping (b) at 80 K for unbiased conditions.
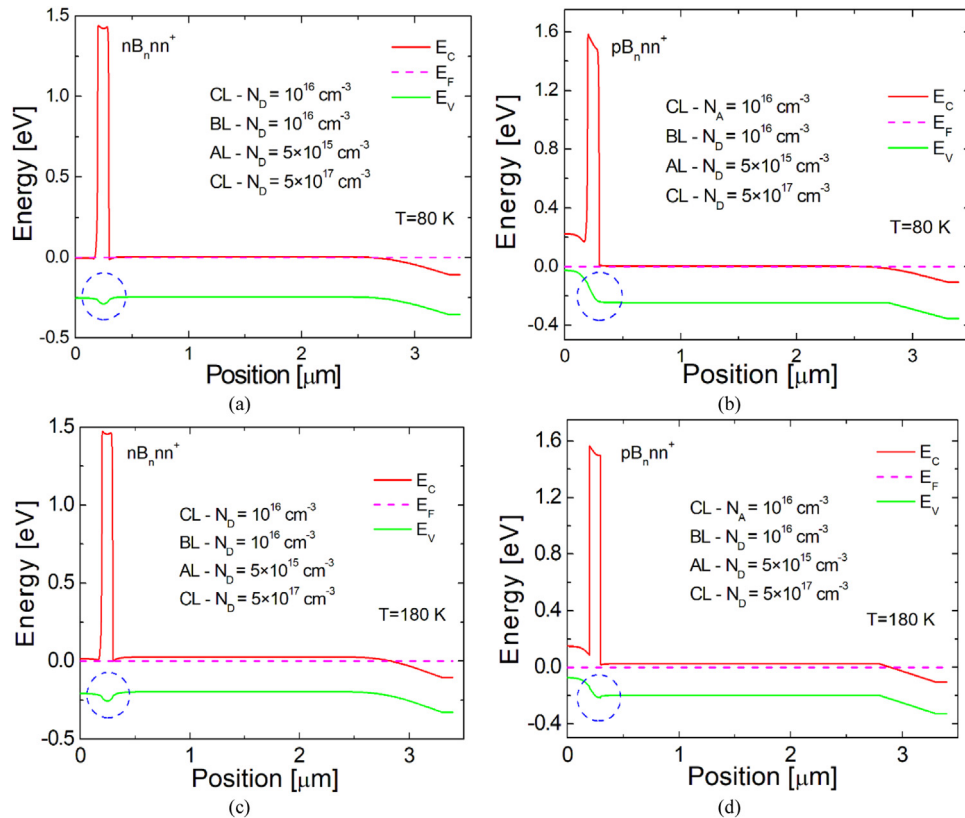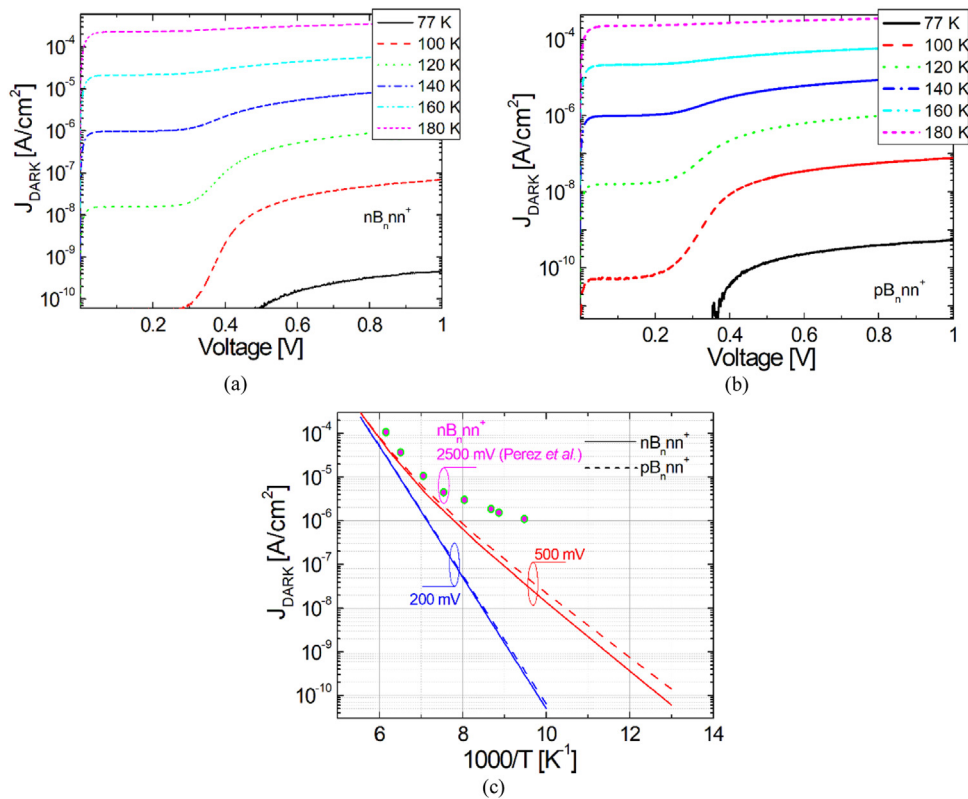

Fig. 6. Calculated energy levels diagram for MWIR T2SLs InAs/InAsSb/B-AlAsSb barrier structure for two XBn detector's architectures: nB_nnn^+ (a, c) and pB_nnn^+ (b, d) for unbiased condition simulated at T =80 K and 180 K.

Fig. 7. Dark current for detector's architectures: nB_nnn^+ (a) and pB_nnn^+ (b) *vs.* voltage for selected temperatures: 77–180 K and *vs.* reciprocal temperature and selected voltages: 200 and 500 mV (c). Experimental results were presented after Perez *et al.* for $V = 2500$ mV [9].
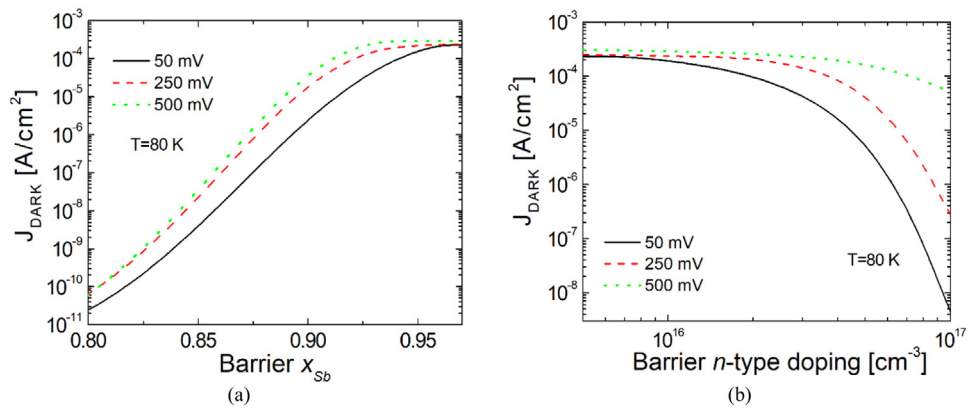
Fig. 8. Dark current for nB_nnn^+ detector *vs.* barrier x_{Sb} (a) and barrier n-type doping (b) at 80 K and selected voltages 50, 250, 500 mV.
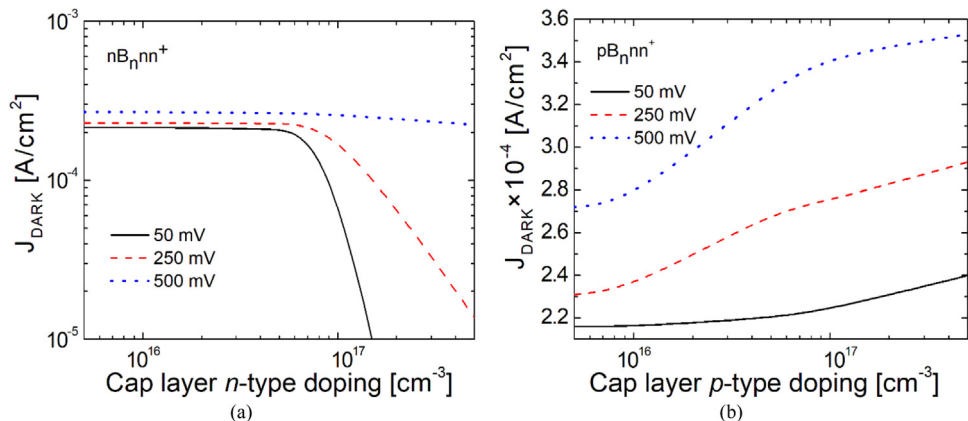
Fig. 9. Dark current for nB_nnn^+ detector *vs.* n/p-type cap layer doping N_D (a) and pB_nnn^+ *vs.* cap layer doping N_A (b) at 180 K and selected voltages 50, 250, 500 mV.
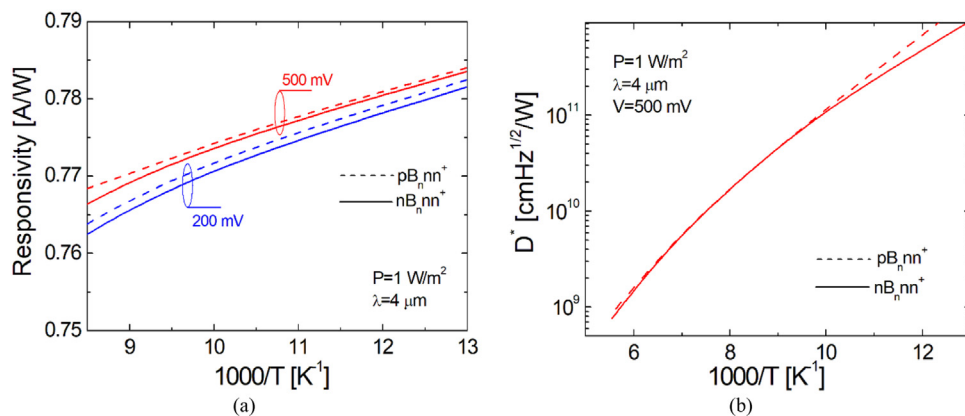
Fig. 10. Responsivity (a) and detectivity (b) for two detector's architectures: nB_nnn^+/pB_nnn^+ vs. reciprocal temperature and selected voltages: 200 mV and 500 mV.
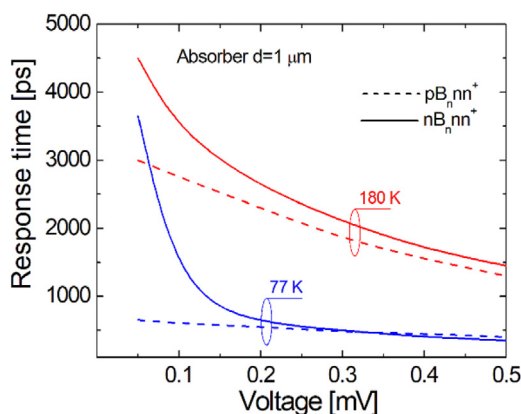

Fig. 11. Response time for two detector's architectures: nB_nnn^+ and pB_nnn^+ vs. voltage and selected temperatures: 77 K and 180 K.

to our simulation the barrier in valence band for $x_{Sb} = 0.97$ and $N_D = 10^{17}$ cm^{-3} should assume $E_V \sim 0.4$ eV for the unbiased structure leading to the suppression of the photocurrent and lowering performance. The similar parameters were assumed by Perez et al. for XBn device that requires high voltage, $V \sim 2500$ mV (turn on voltage) to breach barrier in valence band [9].

The cap layer doping influence on E_C and E_V is presented in Fig. 5(a) and Fig. 5(b). Simulations were performed assuming barrier $x_{Sb} = 0.97$ and $N_D = 10^{16}$ cm^{-3}. In order to minimize E_V, the n-type cap layer must meet the doping requirement $N_D < 10^{17}$ cm^{-3} while for the p-type E_V for analyzed doping range ($N_{D/A} = 5 \times 10^{15} - 5 \times 10^{17}$ cm^{-3}) stays within 0 – 0.02 eV.

E_V and E_C analysis is fully confirmed by simulated band profiles. Calculated energy levels for two architectures with different cap layers: nB_nnn^+ and pB_nnn^+ detectors are presented in Figs. 6(a)–6(d) for 80/180 K and unbiased condition, respectively. The T2SLs InAs/InAsSb electron affinity was simulated as an average of InAs and InAsSb ($x_{Sb} = 0.4$). For n-type contact layer an extra barrier in the valence band is visible while the barrier in the conduction band is close to ~ 1.5 eV. Barrier in valence band for nB_nnn^+ at 80 K is ~ 50 meV and for 180 K we observe ~ 60 meV while for pB_nnn^+ the barrier in valence band is visible for 180 K assuming ~ 30 meV.

Dark current (J_{DARK}) characteristics vs. voltage and reciprocal temperature for the two detector architectures: nB_nnn^+ and pB_nnn^+ are presented in Figs. 7(a)–7(c). Since E_C is comparable for two analyzed architectures at 80 K dark current is determined by minority carrier transport assuming difference in the cap layer doping type, $N_D = N_A = 10^{16}$ cm^{-3}. When E_C is compared for analyzed structures the E_V is nearly 10 times higher for nB_nnn^+ in comparison to

pB_nnn^+ leading to the fact that J_{DARK} is slightly higher for pB_nnn^+ structure. The XBn structure presented by Perez et al. reaches dark current, $J_{DARK} \sim 3 \times 10^{-6}$ A/cm^2 within the voltage range 0.5–1 V ($T \sim 180$ K) while comparable structure simulated in our paper assumes $\sim 3 \times 10^{-4}$ A/cm^2 [Fig. 7(a)].

The similar relation is visible for $T \sim 100$ K however both J_{DARK} stays within the range of $10^{-8} - 10^{-7}$ A/cm^2 indicating on E_V barrier optimization [9]. Figure 7(c) presents Arrhenius plots for structure presented by Perez et al. ($V = 2500$ mV) and simulated structure for $V = 200$ mV and 500 mV. These results also confirm the proper barrier optimization in simulated nB_nnn^+ structure.

The dark current dependence on barrier x_{Sb} and n-type doping is presented in Fig. 8(a) and Fig. 8(b) for three selected voltages: 50, 250 and 500 mV. The barrier x_{Sb} dependence on J_{DARK} was simulated assuming $N_D = 10^{16}$ cm^{-3} while the barrier doping influence was estimated for $x_{Sb} = 0.97$.

Antimony composition change in the barrier layer within the range 0.8 – 1.0 leads to the J_{DARK} increase by nearly seven orders of magnitude. The barrier layer doping increase from 5×10^{15} to 10^{17} cm^{-3} reduces J_{DARK} by more than four orders of magnitude. J_{DARK} stays nearly constant for $N_D < 10^{16}$ cm^{-3} being comparable with absorber doping.

Dark current vs. n/p-type cap layer doping for three selected voltages: 50, 250, 500 mV is presented in Fig. 9(a) and Fig. 9(b). Assuming n-type cap layer $N_D > 6 \times 10^{16}$ cm^{-3}, J_{DARK} decreases sharply for 50 and 250 mV while under 500 mV barrier in valence band is breached and J_{DARK} stays constant in analyzed n-type cap layer doping. In case of the p-type cap layer J_{DARK} increases indicating that E_V decreases in analyzed doping range.

Responsivity simulated for $\lambda = 4$ μm and power $P = 1$ W/m^2 vs. reciprocal temperature is presented in Fig. 10(a). Responsivity increases vs. 1/T and voltage. Assuming unity electric gain (g), for $\lambda = 4$ μm and $T = 100$ K, the quantum efficiency (η) is 24% according to the relation: $\eta = \frac{hcR_i}{\lambda qg}$, where h stands for the Planck constant, c is the light speed, q is the electric charge and R_i the current responsivity. Detectivity was calculated assuming Johnson-Nyquist and shot noises contributions according to the relation:

$$D^* = \frac{R_i}{\left(\frac{4k_BT}{RA} + 2qJ_{DARK} \right)^{0.5}}, \tag{7}$$

where: k_B, R, A, stand for the Boltzmann constant, the resistance and detector's electrical area (100×100 μm^2). Scene influence was not included in the simulation. D^* vs. reciprocal temperature was presented in Fig. 10(b). Detectivity decreases vs. voltage and drops almost two orders of magnitude from $\sim 7 \times 10^{11}$ to 10^9 cmHz$^{1/2}$/W within the temperature range of 80 – 190 K ($V = 500$ mV).

Response time was derived of photocurrent dependence on time where time for $\sim 1/e$ drop from photocurrent's maximum value was assessed. The model given by Li and Dutton was used [10]. Response time *vs.* voltage for both nB_nnn^+ and pB_nnn^+ architectures is presented in Fig. 11. Absorber thickness, $d = 1\ \mu m$ was assumed in simulations due to the low carriers mobility and diffusion length [see Fig. 3(a)]. The barrier influence is clearly visible where nB_nnn^+ structure exhibits higher response time for bias < 150 meV. At 77 K temperature response time ranges from 650 to 420 ps. Since electric field mostly drops at the barrier - absorber heterojunction, the response time is influenced by diffusion mechanism. The higher barrier in valence band at 180 K contributes to the longer response time.

3. Conclusions

We demonstrated theoretical modelling of MWIR XBn photodetectors with T2SLs InAs/InAsSb active layer where AlAsSb barrier ($x_{Sb} = 0.97$ and $N_D < 2 \times 10^{16}\ cm^{-3}$) was implemented. It was shown that material does not introduce extra barriers in valence band in analyzed XBn structure in relation to the *n*-type active layer $N_D = 5 \times 10^{15}\ cm^{-3}$. The detectivity of the simulated structure was assessed at the level of $\sim 10^{11}$ Jones for $T \sim 100\ K$. In order to reach high frequency response of ~ 420 ps the active layer must be thinned to the level of $\sim 1\ \mu m$ due to the low carrier mobility and diffusion length in T2SLs InAs/InAsSb active layer.

Acknowledgement

References

[1] D.Z.-Y. Ting, A. Soibel, L. Höglund, J. Nguyen, C.J. Hill, A. Khoshakhlagh, S.D. Gunapala, Type-II superlattice infrared detectors, Semicond. Semimetals 84 (2011) 1–57, http://dx.doi.org/10.1016/B978-0-12-381337-4.00001-2.
[2] D. Lackner, M. Steger, M.L.W. Thewalt, O.J. Pitts, Y.T. Cherng, InAs/InAsSb strain balanced superlattices for optical detectors, material properties and energy band simulations, J. Appl. Phys. 111 (2012), 034507-1–9, http://dx.doi.org/10.1063/1.3681328.
[3] T. Schuler-Sandy, S. Myers, B. Klein, N. Gautam, P. Ahirwar, Z.-B. Tian, T. Rotter, G. Balakrishnan, E. Plis, S. Krishna, Gallium free type II InAs/InAs$_x$Sb$_{1-x}$ superlattice photodetectors, Appl. Phys. Lett. 101 (2012), 071111-1–3, http://dx.doi.org/10.1063/1.4745926.
[4] E.H. Steenbergen, B.C. Connelly, G.D. Metcalfe, H. Shen, M. Wraback, D. Lubyshev, Y. Qiu, J.M. Fastenau, A.W.K. Liu, S. Elhamri, O.O. Cellek, Y.-H. Zhang, Significantly improved minority carrier lifetime observed in a long-wavelength infrared III–V type-II superlattice comprised of InAs/InAsSb, Appl. Phys. Lett. 99 (2011), 251110-1–3, http://dx.doi.org/10.1063/1.3671398.
[5] L. Höglund, D.Z.-Y. Ting, A. Khoshakhlagh, A. Soibel, C.J. Hill, A. Fisher, S. Keo, S.D. Gunapala, Influence of radiative and non-radiative recombination on the minority carrier lifetime in midwave infrared InAs/InAsSb superlattices, Appl. Phys. Lett. 103 (2013), 221908-1–5, http://dx.doi.org/10.1063/1.4835055.
[6] S. Maimon, G.W. Wicks, nBn detector, an infrared detector with reduced dark current and higher operating temperature, Appl. Phys. Lett. 89 (2006), 151109-1-3, http://dx.doi.org/10.1063/1.2360235.
[7] I. Vurgaftman, J.R. Meyer, Band parameters for III–V compound semiconductors and their alloys, J. Appl. Phys. 89 (2001) 5815–5875, http://dx.doi.org/10.1063/1.1368156.
[8] V.O. Turin, A modified transferred-electron high-field mobility model for GaN devices simulation, Solid-State Electron. 49 (10) (2005) 1678–1682, http://dx.doi.org/10.1016/j.sse.2005.09.002.
[9] J.-P. Perez, Q. Durlin, C. Cervera, P. Christol, New Ga-Free InAs/InAsSb superlattice infrared photodetector, In Proceedings of the 6th International Conference on Photonics, Optics and Laser Technology (2018) 232–237, http://dx.doi.org/10.5220/0006634002320237.
[10] Q. Li, R.W. Dutton, Numerical small-signal AC modeling of deep-level-trap related frequency-dependent output conductance and capacitance for GaAs MESFET's on semi-insulating substrates, IEEE Trans. Electron Devices 38 (1991) 1285–1288, http://dx.doi.org/10.1109/16.81618.